Research Square

Preprints are preliminary reports that have not undergone peer review.
They should not be considered conclusive, used to inform clinical practice,
or referenced by the media as validated information.

Mechanism-Informed Computational Design of RNA Aptamers for Unmodified AuNP Colorimetric Sensing of C16-Ceramide

Yiting Li
Nanjing Tech University
Hongyu Chen
Nanjing Tech University
Yaqiong Yang
Nanjing Normal University
Dengming Ming
dming@njtech.edu.cn

Nanjing Tech University

Research Article

Keywords: RNA aptamers, molecular dynamics simulations, gold nanoparticles, colorimetric biosensing, C16-ceramide, mechanism-informed design

Posted Date: November 23rd, 2026

DOI: https://doi.org/10.21203/rs.3.rs-11570079/v1

License: This work is licensed under a Creative Commons Attribution 4.0 International License.
Read Full License

Additional Declarations: No competing interests reported.

Mechanism-Informed Computational Design of RNA Aptamers for Unmodified AuNP Colorimetric Sensing of C16-Ceramide

[1§]Yiting Li[†], [1]Hongyu Chen[†], [2]Yaqiong Yang* and [1]Dengming Ming*

[1] *College of Biotechnology and Pharmaceutical Engineering, Nanjing Tech University, Nanjing 210023, PR China*

[2] *College of Food and Pharmaceutical Engineering, Nanjing Normal University, Nanjing 211816, PR China*

* Corresponding author: Yaqiong Yang (yangyq@njnu.edu.cn), Dengming Ming (dming@njtech.edu.cn)

[§]Now in the Institute of Biopharmaceutical and Health Engineering, Shenzhen International Graduate School, Tsinghua University, Shenzhen 518055, PR China

[†]Equally contributed to this work.

Abstract

Nucleic acid aptamers recognize diverse targets through programmable three-dimensional architectures; however, their practical biosensing performance also depends on biophysical compatibility with downstream signal-transduction platforms. In adsorption-mediated, label-free gold nanoparticle (AuNP) colorimetric assays, functional sensing requires aptamers to coordinate AuNPs in the apo-state and sterically disengage upon target complexation. Here, using C16-ceramide as a model target, we developed a mechanism-informed computational prioritization strategy coupling target affinity with interfacial colloidal physics. Although the top-ranked scaffold RNA052 bound C16-ceramide strongly, deep internal helical encapsulation precluded target-dependent modulation of AuNP adsorption. Targeted loop engineering yielded RNAm4, which reoriented the lipid chains outward to sterically disrupt nucleobase–gold interactions while preserving favorable binding thermodynamics. Colorimetric assays confirmed that RNAm4 elicited target-specific, concentration-dependent optical shifts, whereas RNA052 remained unresponsive. Negative-control assays further supported the importance of considering both predicted binding energetics and ligand presentation. The proposed mechanism-informed workflow can serve as a complement to experimental aptamer discovery and be adaptable to other small-molecule targets, supporting the development of rapid, label-free colorimetric sensing platforms.

Keywords: RNA aptamers, molecular dynamics simulations, gold nanoparticles, colorimetric biosensing, C16-ceramide, mechanism-informed design

Introduction

Aptamers are functional single-stranded oligonucleotides (DNA or RNA) that fold into well-defined three-dimensional architectures to bind designated molecular targets with high affinity and selectivity via non-covalent interactions [1, 2]. Aptamers have been successfully generated against diverse biological targets, ranging from metal ions and small metabolites to macromolecular protein complexes [3-7]. Owing to their synthetic accessibility, ease of chemical modification, high thermal stability, and structural programmability, aptamers have emerged as prominent molecular-recognition elements across diverse biosensing paradigms [8, 9].

Among aptamer-based biosensing platforms, colorimetric assays employing unmodified gold nanoparticles (AuNPs) have gained widespread prominence, offering a simple strategy to convert molecular recognition events into direct visual readouts [10, 11]. This modality leverages the localized surface plasmon resonance (LSPR) of colloidal gold: well-dispersed, citrate-capped AuNPs exhibit an absorption band centered near 520 nm (manifesting as a characteristic wine-red hue), whereas salt-induced aggregation drives interparticle plasmonic coupling and a distinct bathochromic shift toward purple or blue [11]. Mechanistically, this assay relies on a tunable interfacial adsorption equilibrium. In the absence of target, flexible single-stranded aptamers adsorb onto the AuNP surface through cooperative coordinate contacts between unstacked nucleobases and gold facets, conferring electrostatic and steric resistance against electrolyte-induced aggregation [12, 13]. Upon target binding, adaptive folding or steric reorientation is postulated to attenuate nucleobase–gold coordination, rendering the nanoparticles vulnerable to salt challenge and triggering target-dependent aggregation [14].

Target-specific aptamers are traditionally generated using systematic evolution of ligands by exponential enrichment (SELEX), in which a large randomized nucleic-acid library undergoes repeated cycles of target binding, partitioning, amplification, and enrichment [15]. Although SELEX remains a widely used route for aptamer discovery, conventional workflows can be labor-intensive and time-consuming. Computational strategies have therefore increasingly been explored

to assist or complement experimental aptamer development. For computational prioritization schemes intended for adsorption-based AuNP colorimetric sensing, favorable target binding alone does not necessarily ensure effective signal generation. Because this sensing format does not rely on additional chemical modification, successful detection requires not only specific aptamer-target recognition but also appropriate modulation of the aptamer-AuNP interface after target binding. Therefore, understanding the interactions among the aptamer, target, and citrate-capped AuNPs is important for selecting aptamer suitable for this type of colorimetric system.

C16-ceramide [Cer(d18:1/16:0)] is a long-chain ceramide species involved in sphingolipid metabolism and cellular signaling, with its altered circulating level reported in cognitive decline and dementia [16]. An early lipidomics study identified increased plasma C16-ceramide in patients with Alzheimer's disease (AD) compared with cognitively normal controls [17], while a large prospective 2024 cohort study involving 4488 older adults found that higher circulating C16-ceramide was associated with an increased risk of incident dementia [18]. These findings suggest that C16-ceramide may serve as a potential disease-associated indicator and highlight the need for selective detection methods.

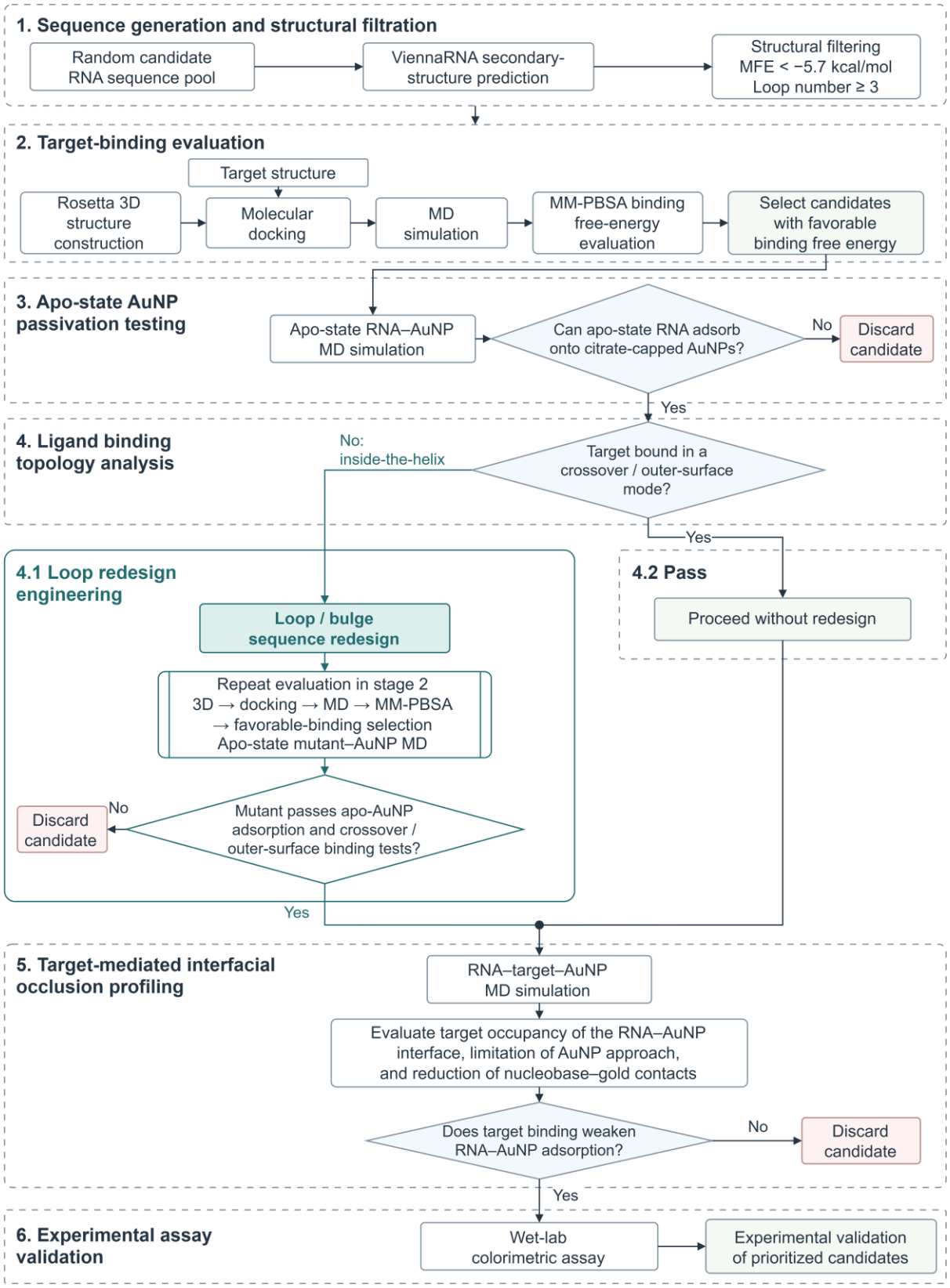
Here, we report a mechanism-informed computational strategy to prioritize and rationally remodel RNA aptamers for label-free AuNP-based colorimetric biosensing, using C16-ceramide as a model target. We show that successful signal transduction depends not only on target-binding affinity, but also on the topological presentation of the bound ligand and its ability to sterically regulate AuNP surface passivation. Through loop-directed sequence engineering, we successfully repositioned the ceramide hydrocarbon chains toward the solvent-accessible perimeter while retaining favorable binding thermodynamics. By coupling molecular recognition with interfacial colloidal physics, this work highlights the indispensable value of designing aptamer probes in direct alignment with their downstream sensing mechanism.

Materials and methods

Computational and Experimental Workflow Overview

We organized a mechanism-informed computational workflow to prioritize RNA aptamers for label-free, unmodified AuNP-based colorimetric biosensing. Departing from conventional affinity-only docking paradigms, this framework couples target binding thermodynamics with interfacial colloidal surface chemistry. The pipeline encompasses six integrated phases: (i) *sequence generation and structural filtration*, involving randomized 29-mer sequence generation and secondary-structure complexity screening; (ii) *target-binding evaluation*, combining 3D structural modeling, molecular docking, all-atom MD simulations, and MM-PBSA free energy calculations; (iii) *apo-state AuNP passivation testing*, assessing non-covalent adsorption and colloidal stabilization on citrate-capped AuNPs; (iv) *ligand-binding topology analysis and loop engineering*, resolving target display and remodeling buried conformations; (v) *target-mediated interfacial occlusion profiling*, verifying whether target binding sterically obstructs AuNP surface approach; and (vi) *experimental assay validation*, examining prioritized aptamers via AuNP colorimetric assays to verify target-dependent plasmonic responses. Technical specifications are detailed in the following subsections.

Scheme 1. Computational workflow for selecting aptamer suitable for AuNP-based colorimetric sensing.


1. Sequence generation and structural filtration
Random candidate RNA sequence pool
ViennaRNA secondary-structure prediction
Structural filtering MFE < −5.7 kcal/mol Loop number ≥ 3
2. Target-binding evaluation
Target structure
Rosetta 3D structure construction
Molecular docking
MD simulation
MM-PBSA binding free-energy evaluation
Select candidates with favorable binding free energy
3. Apo-state AuNP passivation testing
Apo-state RNA–AuNP MD simulation
Can apo-state RNA adsorb onto citrate-capped AuNPs?
No
Discard candidate
Yes
4. Ligand binding topology analysis
No: inside-the-helix
Target bound in a crossover / outer-surface mode?
Yes
4.1 Loop redesign engineering
Loop / bulge sequence redesign
Repeat evaluation in stage 2 3D → docking → MD → MM-PBSA → favorable-binding selection Apo-state mutant–AuNP MD
Mutant passes apo-AuNP adsorption and crossover / outer-surface binding tests?
No
Discard candidate
Yes
4.2 Pass
Proceed without redesign
5. Target-mediated interfacial occlusion profiling
RNA–target–AuNP MD simulation
Evaluate target occupancy of the RNA–AuNP interface, limitation of AuNP approach, and reduction of nucleobase–gold contacts
Does target binding weaken RNA–AuNP adsorption?
No
Discard candidate
Yes
6. Experimental assay validation
Wet-lab colorimetric assay
Experimental validation of prioritized candidates

113

Generation of Three-Dimensional Structures

Horii et al. demonstrated that an 80-nucleotide SPC-binding RNA aptamer could be truncated to 33 nucleotides while retaining a conserved 10-nucleotide hairpin motif implicated in SPC recognition and binding affinity [19]. Inspired by the feasibility of such compact aptamer scaffolds, we selected a 29-nucleotide length and generated a library of 200 random sequences for subsequent computational screening against C16-ceramide. Subsequently, the minimum free-energy (MFE) secondary structure of each sequence was predicted using the ViennaRNA package [20]. We retained sequences with predicted MFE $\leq -5.7\ \mathrm{kcal} \cdot \mathrm{mol}^{-1}$ for three-dimensional RNA modeling using the FARFAR2 [21] protocol in Rosetta, using the predicted secondary structures as modeling restraints.

We retrieved the two-dimensional structure of C16-ceramide from PubChem [22] and converted it into an initial three-dimensional model using Chem3D. The resulting geometry was energy-minimized using the MM2 force field [23] to generate the ligand structure for subsequent calculations.

Molecular Docking

Molecular docking of C16-ceramide with the candidate RNA aptamers was performed using AutoDock Vina (version 1.2.0) [24]. Receptor and ligand structures were parameterized with polar hydrogens and Gasteiger partial charges using AutoDockTools [25]. Putative binding pockets were predicted using the dynamics perturbation analysis (DPA) algorithm [26] to center the cubic search grid. An exhaustiveness value of 32 was used to ensure thorough conformational sampling. Docking conformations were ranked by Vina binding scores and then visually inspected in PyMOL (version 2.5) for non-covalent contacts (hydrogen bonds and hydrophobic packing). The most energetically favorable pose with optimal structural complementarity was selected as the initial

coordinate for downstream molecular dynamics (MD) simulations.

MD Simulations of RNA-ceramide Complexes

MD simulations of the RNA-ceramide complexes were conducted using GROMACS 2021 [27]. The RNA aptamer was parameterized with the AMBER ff99bsc0χOL3 force field [28, 29], while C16-ceramide parameters were generated using GAFF2 [30] with AM1-BCC charges [31]. Each complex was centered in a cubic box and solvated with TIP3P water molecules [32], ensuring a minimum distance of 1.0 nm between the solute and the box boundaries. To neutralize the net charge and mimic physiological ionic strength (~0.15 M), 54 Na^+ and 24 Cl^- ions were introduced to the system. Energy minimization was initially performed using the steepest descent algorithm to eliminate steric clashes. Subsequently, the system equilibrated for 100 ps under the NVT ensemble at 300 K using the V-rescale thermostat, followed by another 100 ps equilibration under the NPT ensemble at 300 K and 1 bar using the Parrinello-Rahman barostat. Finally, production MD simulations were carried out for 150 ns with an integration time step of 2 fs. Long-range electrostatic interactions were treated using the Particle Mesh Ewald (PME) [33] method, and covalent bonds involving hydrogen atoms were constrained using the LINCS [34] algorithm.

Binding Free Energy Calculations and Hydrogen-Bond Analysis

Binding energetics were evaluated using the MM-PBSA method implemented in g_mmpbsa package of GROMACS [35-37]. The binding energy was calculated as the sum of the van der Waals, electrostatic, polar solvation, and nonpolar solvation contributions. The polar solvation contribution was calculated by solving the linearized Poisson–Boltzmann equation with solute and solvent dielectric constants of 2 and 80, respectively, at 300 K, with monovalent cations and anions each assigned a bulk concentration of 0.150 M. The nonpolar solvation contribution was estimated using

$$G_{\mathrm{SASA}} = \gamma\,\mathrm{SASA} + b$$

with $\gamma = 0.0054\,\mathrm{kcal}\cdot\mathrm{mol}^{-1}\cdot\mathrm{Å}^{-2}$ and $b = 0.92\,\mathrm{kcal}\cdot\mathrm{mol}^{-1}$, and a solvent probe radius of 1.4 Å. A single-trajectory protocol was employed, in which the coordinates of the RNA aptamer and ligand were extracted from the corresponding complex trajectory. Following correction for periodic boundary conditions, 2000 snapshots were extracted at uniform intervals of 50 ps from the last 100 ns of each production trajectory. The reported values are entropy-uncorrected MM-PBSA binding energy estimates and were used to compare the complexes.

Intermolecular hydrogen bonds between the RNA aptamer and C16-ceramide were analyzed using the gmx hbond tool in GROMACS. A hydrogen bond was defined based on standard geometric criteria: a donor–acceptor distance cutoff of ≤ 0.35 nm and a donor–hydrogen–acceptor angle cutoff of $\geq 120°$. The hydrogen-bond occupancy over the final 100 ns was computed to identify the persistent contact residues stabilizing the RNA–ligand complex.

MD Simulations of RNA-AuNP and RNA-ceramide-AuNP systems

Gold nanoparticles (AuNPs) were modeled atomistically following the parameterization and structural methodology described by Phanchai et al [12]. Each nanoparticle had a diameter of approximately 3 nm and contained 459 Au atoms arranged in a face-centered cubic (FCC) lattice with a truncated octahedral morphology. Gold atoms carried zero partial charge, and nonbonded interactions were modeled via a standard 12–6 Lennard–Jones potential:

$$U_{ij}(r) = 4\varepsilon_{ij}\left[\left(\frac{\sigma_{ij}}{r}\right)^{12} - \left(\frac{\sigma_{ij}}{r}\right)^{6}\right]$$

with Au parameters of $\sigma_{\mathrm{Au}} = 0.2629$ nm and $\varepsilon_{\mathrm{Au}} = 22.133\mathrm{kJ}\cdot\mathrm{mol}^{-1}$ as reported in Table S1 of the Supporting Information of Phanchai et al. Cross-interaction parameters between Au and all other atom types were determined using standard Lorentz–Berthelot combination rules. The nanoparticle surface was coated with 10 citrate molecules in a divalent state (net charge of $-2.0\,e$ per citrate, protonated at the central carboxylate group), parameterized using an AMBER-

compatible force field with partial charges derived from quantum chemical electrostatic surface potential fits (HF/6-31G* via ANTECHAMBER [38]). During the simulations, the Au atoms, citrate molecules, and aptamer were allowed to move dynamically under the force field. The simulated system was solvated in a periodic cubic box of approximately $12.0 \times 12.0 \times 12.0\ \mathrm{nm}^3$ using explicit SPC/E [39] water molecules. The RNA aptamer was parameterized using the AMBER03 force field. Counterions were added to ensure strict electroneutrality and to yield a physiological ionic strength of approximately $0.15\ \mathrm{mol} \cdot \mathrm{L}^{-1}$ NaCl. All molecular dynamics simulations were carried out using GROMACS 2021. The system was energy-minimized using the steepest descent algorithm, followed by NVT equilibration at 300 K and subsequent NPT equilibration at 300 K and 1.0 bar. Production simulations were run for 5 ns with a 2-fs integration time step. The temperature was maintained at 300 K using the velocity-rescaling thermostat with a time constant $\tau_t = 0.1\ \mathrm{ps}$ (coupling solute and solvent/ions separately). The pressure was maintained isotropically at 1.0 bar using the Parrinello–Rahman barostat with a coupling time constant $\tau_p = 2.0\ \mathrm{ps}$ and an isothermal compressibility of $4.5 \times 10^{-5}\ \mathrm{bar}^{-1}$. All chemical bonds involving hydrogen atoms were constrained using the LINCS [34] algorithm, and water geometries were kept rigid using the SETTLE [40] algorithm.

The simulation setup and execution for the RNA–ceramide–AuNP system were kept identical to those used for the RNA–AuNP system. The C16-ceramide ligand was parameterized using AmberTools (Antechamber/GAFF with HF/6-31G* RESP [41] charges via ACPYPE [42]) and pre-complexed with the 29-nt RNA aptamer. The complex was embedded in an expanded cubic box, $15.0 \times 15.0 \times 15.0\ \mathrm{nm}^3$ solvated with SPC/E water molecules, neutralized, and provided with ~0.15 M NaCl. Nonbonded cutoffs, integration, and temperature/pressure control algorithms strictly matched those used for the RNA–AuNP simulation.

AuNP-based Colorimetric Assay

Preparation of AuNPs: Citrate-stabilized AuNPs (~13 nm) were prepared via the

standard Turkevich–Frens method using aqua regia-cleaned glassware [43, 44]. Briefly, an aqueous $HAuCl_4$ solution (80 mL, 1.0 mM) was heated to reflux under vigorous stirring. Sodium citrate solution (8.0 mL, 38.8 mM) was rapidly injected into the boiling mixture, prompting a distinct color transition to deep wine-red. Stirring and boiling were maintained for 15 min, then the heating source was removed, and the colloid was cooled to room temperature under continuous stirring. The resulting suspension was passed through a 0.22 μm PES membrane and stored in the dark at 4°C.

RNA Preparation and Thermal Annealing: The RNA aptamer was purchased from Genscript Biotechnology Co., Ltd. (Nanjing, China) and reconstituted in RNase-free buffer. Before the assays, the RNA solution underwent thermal denaturation and renaturation to promote proper tertiary folding and ensure a functional conformation. Briefly, the solution was incubated at 85°C for 10 min to melt intermolecular misfolded structures, rapidly cooled at 4°C for 10 min, and finally equilibrated at room temperature (~25°C) for 10 min. Freshly folded RNA was used immediately for subsequent binding and colorimetric experiments.

Colorimetric Assay: AuNP suspension (360 μL, 2.4 nM) was incubated with folded RNA aptamer (20 μL, 8.0 μM) for 30 min at room temperature to allow aptamer adsorption. For target detection, 20 μL of target in PBS at the indicated concentrations was added and incubated for 15 min. Then, 30 μL of 0.15 M NaCl was added and incubated for 10 min to induce salt-mediated AuNP aggregation. The colorimetric response was monitored by visual inspection and quantified by UV–visible spectroscopy.

UV-visible (UV-vis) spectroscopy: UV–vis spectra of the AuNP suspensions were recorded over 400–800 nm using a Hitachi UH-5300 spectrophotometer (Hitachi High-Tech, Tokyo, Japan). Baseline correction was conducted using the reaction buffer. UV-vis data processing and plotting were performed using GraphPad Prism 9. Nanoparticle formation and dispersion stability were verified by this UV-vis spectroscopy, exhibiting a characteristic localized surface plasmon resonance (LSPR) peak at $\lambda_{max} = 520$ nm [45].

Results and discussion

Computational Modeling and Characterization of RNA-Ceramide Complexes

As the first step in our design framework, we selected candidate RNA aptamers with potential C16-ceramide recognition (Fig. 1A). To delineate sequence length and constrain the conformational search space, we referred to an established aptamer targeting sphingosylphosphorylcholine [19]—a structural analogue of C16-ceramide sharing long hydrophobic aliphatic chains and polar functional groups ($-\mathrm{OH}$ and $-\mathrm{NH_2}$) (Fig. 1B). Based on this length constraint, an *in silico* library containing 200 random 29-mer RNA sequences was generated, and their minimum free energy (MFE) secondary structures were predicted using the ViennaRNA package (RNAfold). Because high-affinity, specific small-molecule recognition generally requires preorganized structural architectures [46], we applied two structural-complexity criteria: a minimum folding free energy (ΔG_{MFE}) below $-5.7\ \mathrm{kcal \cdot mol^{-1}}$ and a loop count of ≥ 3. This enrichment strategy effectively filtered out unstable and poorly structured sequences, yielding 27 top-ranked RNA candidates for subsequent 3D tertiary structure modeling and molecular docking simulations (Fig. S1).

The three-dimensional structures of the resulting RNA sequences were subsequently generated using the Rosetta software suite. Molecular docking calculations were carried out to elucidate the intermolecular binding geometries between RNA and C16-ceramide. Based on the spatial orientation and topological packing of the ceramide aliphatic chains relative to the nucleic acid framework, the predicted complexes converged into three distinct binding modes: (i) an inside-the-helix mode (Fig. 1C), where both hydrophobic aliphatic chains of C16-ceramide were deeply embedded into the internal helical cavity or core base-stacking pocket; (ii) a crossover mode (Fig. 1D), in which the two aliphatic chains straddled the RNA phosphodiester backbone and partitioned onto opposite solvent-exposed faces; and (iii) an outer-surface mode (Fig. 1E), characterized by superficial adsorption of the ceramide molecule along the peripheral groove surface of the RNA scaffold. Statistical profiling of the 27 RNA–ceramide complexes demonstrated that the inside-

the-helix architecture was predominant, identified in 15 complexes (55.56%), whereas the crossover and outer-surface geometries each accounted for 6 complexes (22.22%).

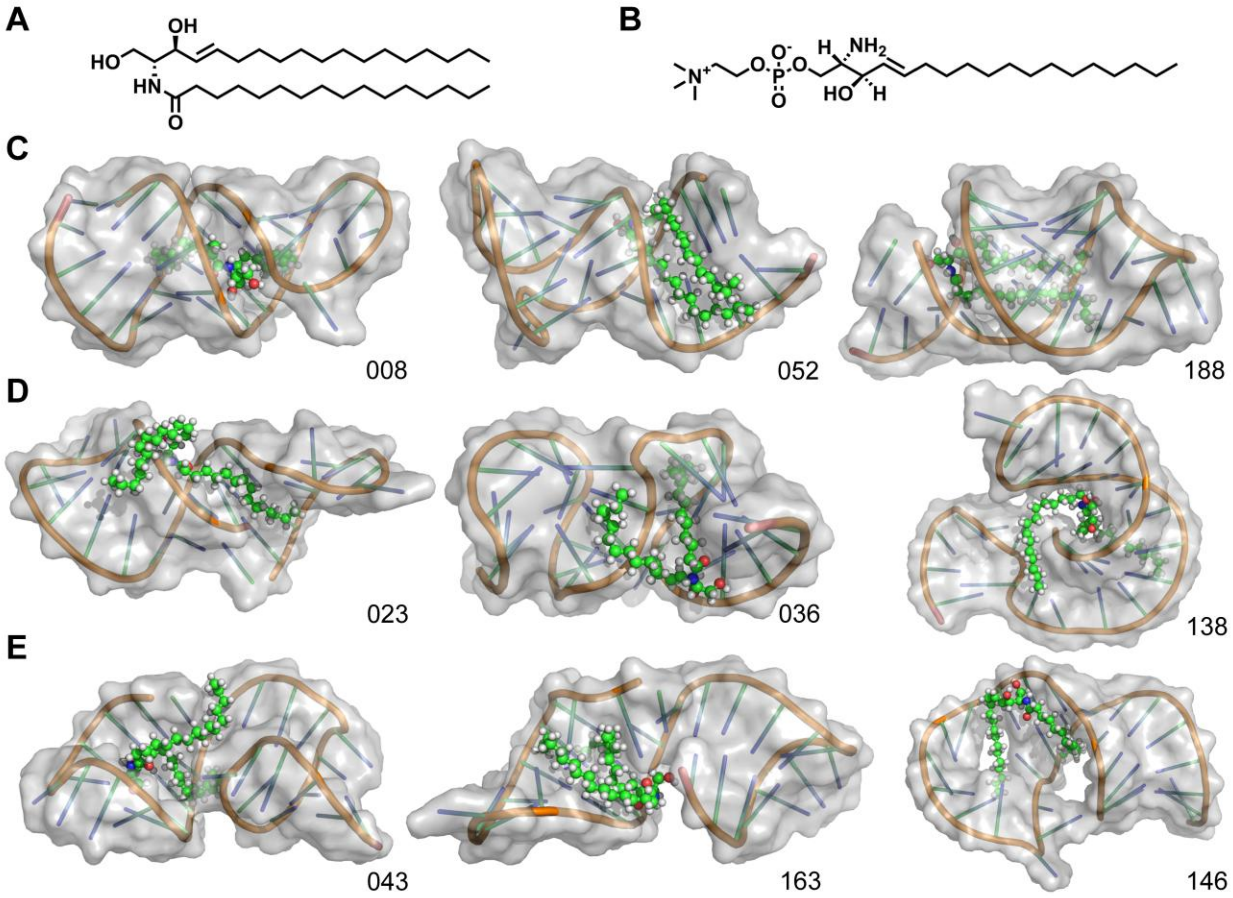


Fig. 1 Docking the ligand with candidate RNA. (A) Chemical structure of C16-ceramide. (B) Chemical structure of Sphingosylphosphorylcholine. (C)-(E) Representative binding conformations between RNA and C16-ceramide in molecular docking: inside-the-helix mode (C), crossover mode (D), and outer-surface mode (E).

To determine whether docking modes correlate with binding favorability, 14 representative RNA-ceramide complexes covering all three geometry types were selected for 150 ns MD simulations. MM-PBSA binding free energies (ΔG_{bind}) were then calculated over the 100-150 ns interval trajectories (Table 1). Among the tested complexes, RNA052 yielded the lowest ΔG_{bind},

suggesting strong C16-ceramide binding. MD analysis revealed hydrogen-bond interactions between C16-ceramide and RNA (Fig. S2). Interestingly, no clear association was observed between the MM-PBSA binding free energies and the three docking-derived binding geometries. This divergence suggests that thermodynamic affinity and ligand-binding topology are two complementary criteria in aptamer selection: while ΔG_{bind} estimates the energetic favorability of complex formation, binding geometry dictates the spatial exposure of the lipid tails relative to the RNA backbone. For AuNP-based colorimetric aptasensors, strong target binding is necessary but not sufficient to drive surface displacement and salt-induced aggregation.

Table 1. Calculated binding free energies ($kJ \cdot mol^{-1}$) of candidate RNA sequences complexed with C16-ceramide evaluated by MM-PBSA over the equilibrated 100–150 ns trajectory window.

Docking types	Number	ΔG_{vdw}	ΔG_{ele}	ΔG_{ps}	ΔG_{nps}	ΔG_{bind}
Inside the helix	052	-253.528	-59.99	16.633	-21.999	-319.531(±13.026)
	013	-218.44	-101.692	75.564	-20.602	-264.918（±12.932）
	084	-136.506	-128.427	41.833	-12.999	-235.984（±11.33）
	124	-180.147	-38.032	37.528	-17.862	-199.025（±9.398）
	189	-152.961	-99.7	78.705	-15.756	-189.145（±10.283）
	030	-145.384	-95.556	76.03	-13.659	-178.528（±14.01）
	188	-87.663	-27.8	21.315	-8.805	-102.985（±16.35）
	056	-101.234	-25.614	59.202	-10.801	-78.367（±22.364）
	057	-0.013	-5.07	24.15	-0.007	19.239（±20.139）
	008	0	0.012	26.433	-0.164	26.664（±12.7）
	152	0	0.371	32.126	-0.035	31.691(±15.311)
Outer surface	163	-212.676	-121.369	80.274	-20.164	-273.459（±11.556）
	043	-214.676	-52.443	30.627	-20.825	-256.758（±17.495）
Crossover	023	0	-1.285	23.635	-0.139	23.353（±14.945）

ΔG_{vdw}: Van der Waals energy; ΔG_{ele}: electrostatic energy; ΔG_{ps}: polar solvation free energy; ΔG_{nps}: nonpolar solvation free energy; ΔG_{bind}: total binding free energy. All values represent mean ± SD.

Evaluation of Apo-State RNA–AuNP Interfacial Adsorption and Colloidal Stabilization

Our computational screening showed that ligand-bound geometry is an essential structural descriptor that affinity rankings alone cannot predict. For colorimetric biosensing, an RNA aptamer must do more than bind its target with high thermodynamic affinity: it must dynamically regulate colloidal gold stability through target-dependent interfacial adsorption. Because colloidal AuNPs (~13 nm in diameter) are sterically excluded from the compact internal helical fold of a structured aptamer, interfacial RNA–AuNP interactions occur almost exclusively along solvent-accessible peripheral domains. In the absence of target, non-covalent adsorption of the flexible, single-stranded apo-aptamer onto citrate-capped AuNPs provides electrostatic and steric stabilization against salt-induced aggregation. Under this adsorption-mediated mechanism, a functional aptamer must bind its target in a way that sequesters its nucleobases or reorganizes its outer surface, thereby attenuating AuNP adsorption and permitting salt-mediated aggregation. Given that oligonucleotide adsorption onto citrate-stabilized gold surfaces is governed by a delicate competition among electrostatic repulsion with surface citrates, local citrate redistribution, and short-range nucleobase–gold coordination [47, 48], we performed all-atom MD simulations of the apo-RNA–AuNP interface to evaluate whether candidate aptamers provide sufficient surface protection prior to target encounter.

RNA052 was selected as a representative binding-competent scaffold to investigate these interfacial dynamics. To probe orientation-dependent binding across the entire solvent-accessible perimeter, 20 independent initial configurations were generated by randomly placing citrate-capped AuNPs around apo-RNA052 at a uniform initial minimum distance of 1.5 Å. Despite this identical initial separation, subsequent binding trajectories diverged markedly depending on the initial approach orientation (Fig. 2A). Approximately 50% of the sampled orientations favored spontaneous, stable RNA–AuNP association, whereas the remaining trajectories resulted in interfacial disengagement. In the 8A-052 configuration, where the AuNP was initially positioned adjacent to residue 8A, time-dependent distances between individual nucleobases and the citrate-capped AuNP surface revealed that several exposed purine bases rapidly established and

maintained close contacts with the gold surface (Fig. 2B). This surface-protective capability was validated experimentally: while unmodified citrate-capped AuNPs rapidly aggregated upon exposure to NaCl (transitioning visually from wine-red to blue), AuNPs pre-incubated with apo-RNA052 remained well dispersed and red under the same ionic strength (Fig. 2C). These experimental observations support our simulation-based conclusion that apo-RNA052 acts as an effective colloidal stabilizer.

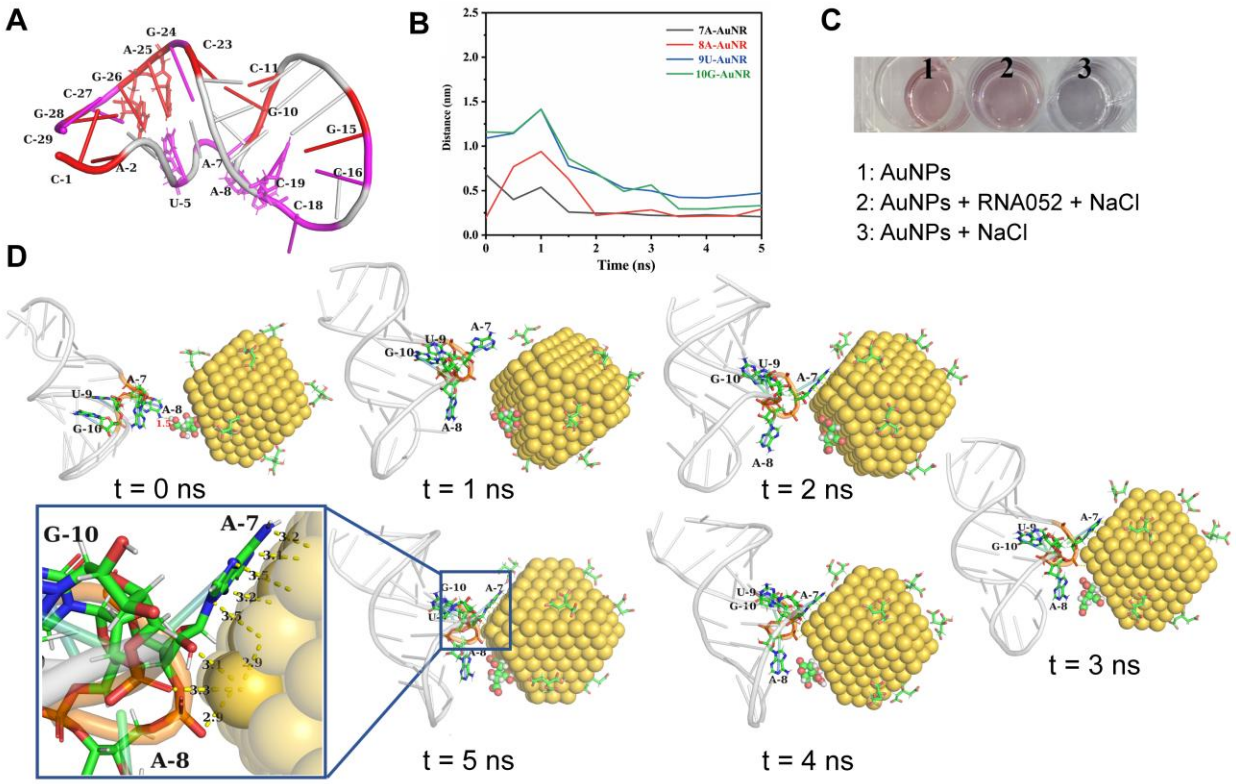


Fig. 2 Interfacial MD simulations and colloidal stabilization of apo-RNA052 on AuNPs. (A) Contact profile between apo-RNA052 and AuNPs across 20 independent 5-ns trajectories (initial minimum separation of 1.5 Å). Red: non-binding regions; purple: binding-permissive regions; gray: unsampled areas. (B) Minimum distance profiles between representative RNA052 nucleobases and the AuNP surface over the 5-ns simulation of the 8A-052 configuration. (C) Visual colorimetric responses of AuNP solutions: bare AuNPs, AuNPs + RNA052 + NaCl

(dispersed), and AuNPs + NaCl (aggregated). (D) Structural snapshot of the 5-ns MD simulation for the apo-RNA052–AuNP complex initiated near residue 8A.

We further dissected interfacial behavior by contrasting two representative orientations: the binding-competent 8A-052 configuration (AuNP near base 8A) and the non-binding 11C-052 configuration (AuNP near base 11C). In the simulation, initial electrostatic repulsion between the anionic RNA backbone and citrate ligands drove interfacial separation and local citrate redistribution. In the 8A-052 case, subsequent conformational reorganization oriented nucleobase N and O atoms toward exposed gold atoms, establishing stable coplanar Au–N/Au–O contacts that promoted stable adsorption (Fig. 2D), consistent with the known propensity of nucleobases to coordinate gold facets in a coplanar fashion [48, 49]. In contrast, the 11C-052 configuration lacked this conformational flexibility, disfavoring surface adsorption due to uncompensated electrostatic repulsion (Fig. S3). Together, these simulations suggest that apo-state RNA adsorption onto citrate-capped AuNPs is orientation-dependent and develops progressively over time. As Brownian motion allows AuNPs and RNA molecules to encounter each other from different orientations in solution, profiling apo-state RNA–AuNP interactions across multiple initial configurations provide a useful criterion for assessing the potential of candidate RNAs to adsorb onto AuNP surfaces and contribute to colloidal stabilization prior to target binding.

Mechanism-Informed Engineering of the Loop Scaffold Balances Target Affinity with Interfacial AuNP Occlusion

Interfacial MD simulations of the apo-state RNA–AuNP complex demonstrated that non-covalent adsorption onto citrate-capped AuNPs relies critically on close nanoparticle approach accompanied by direct nucleobase–gold coordination contacts. This biophysical insight prompted us to systematically reassess the three distinct RNA–ceramide binding geometries identified during our initial docking screen. Notably, the predominant inside-the-helix binding mode

appeared inherently disadvantageous for target-mediated modulation of RNA–AuNP interactions. Because the ceramide ligand is deeply buried within the compact internal helical core, it leaves the peripheral solvent-accessible surface of the RNA largely unperturbed, thereby failing to sterically impede subsequent AuNP approach. This structural constraint did not rule out ligand recognition *per se*, but served as a crucial criterion for AuNP-directed sensor design. Consequently, computational candidates can be optimized via two alternate pathways: direct screening of native sequences that fortuitously balance favorable binding free energies with outward ligand presentation, or rational scaffold remodeling of a high-affinity parent aptamer to selectively redirect target display while preserving binding potency.

Here, we pursued the scaffold-guided optimization route utilizing RNA052 as the parent framework. Although RNA052 exhibited the most favorable predicted RNA–ceramide binding free energy among the candidate pool (Table 1), it sequestered the aliphatic chains of C16-ceramide almost entirely inside the helical groove (Fig. 1C). As illustrated in Fig. 3A, RNA binding pockets for hydrophobic small molecules are predominantly organized around unpaired loop and bulge motifs, which confer structural plasticity and define accessible tertiary cavities. We therefore targeted the flexible loop 2 region of RNA052 for sequence remodeling. Three rationally mutated scaffolds were engineered by modifying the conserved AAU motif within loop 2: RNAm2 (deletion mutant, $\mathrm{AAU} \rightarrow \mathrm{AU}$), RNAm3 (insertion mutant, $\mathrm{AAU} \rightarrow \mathrm{AAAU}$), and RNAm4 (transposition mutant, $\mathrm{AAU} \rightarrow \mathrm{AAUA}$)

These engineered candidates were subjected to molecular docking followed by rigorous MM-PBSA binding free energy evaluation over the equilibrated 100–150 ns trajectory segment (Table 2). Docking poses revealed that both RNAm3 (Fig. 3C) and RNAm4 (Fig. 3D) adopted an outward-oriented binding topology, wherein the hydrophobic alkyl chains projected prominently toward the exterior solvent boundary of the RNA scaffold. However, MM-PBSA energetic decomposition revealed an acute trade-off: RNAm3 yielded an unfavorable positive binding free energy ($\Delta G_{bind} = +1.330\ \mathrm{kJ \cdot mol^{-1}}$), reflecting a compromised binding pocket and unstable ligand retention. Conversely, while RNAm2 retained robust binding affinity ($\Delta G_{bind} =$

$-286.397\ \text{kJ}\cdot\text{mol}^{-1}$), its ligand-binding pose failed to provide sufficient outward surface display (Fig. 3B). Strikingly, RNAm4 successfully reconciled these competing demands, maintaining a strongly favorable binding free energy ($\Delta G_{bind} = -249.067\ \text{kJ}\cdot\text{mol}^{-1}$, dominated by van der Waals interactions $\Delta G_{vdw} = -204.648\ \text{kJ}\cdot\text{mol}^{-1}$) while adopting an outward-oriented target topology (Table 2, Fig. 3D). RNAm4 was consequently selected for downstream comparative AuNP interfacial interrogation.

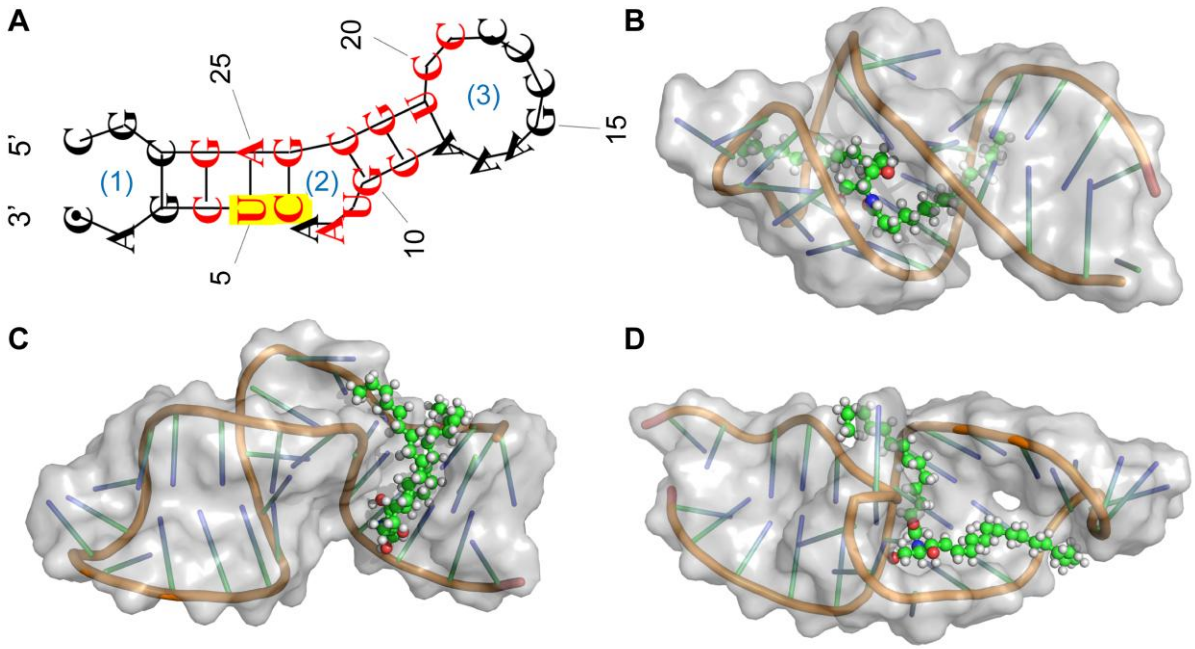


Fig. 3 Redesign of RNA052 to optimize ligand positioning in aptamer candidates. (A) Secondary structure diagram of RNA052 (Red font: the distance between the base and C16-ceramide in this region is within 3.5 angstroms; highlighted in yellow: the base forms a hydrogen bond with C16-ceramide; blue annotations: loop structures). (B)-(D) Binding conformations between C16-ceramide and RNA052 mutants m2 (B), m3 (C), m4 (D) in molecular docking.

Table 2. Thermodynamic binding free energy components ($\text{kJ}\cdot\text{mol}^{-1}$) of C16-ceramide complexed with parent RNA052 and engineered mutants calculated by MM-PBSA over the equilibrated 100–150 ns window.

Number	ΔG_{vdw}	ΔG_{ele}	ΔG_{ps}	ΔG_{nps}	ΔG_{bind}
052	-253.528	-59.99	16.633	-21.999	-319.531(±13.026)
m2	-239.513	-70.247	44.450	-21.207	-286.397（±12.795）
m3	-0.002	-2.710	3.179	-0.119	1.330（±19.889）
m4	-204.648	-43.193	18.072	-19.124	-249.067（±9.678）

405 ΔG_{vdw}: Van der Waals energy; ΔG_{ele}: electrostatic energy; ΔG_{ps}: polar solvation free energy;
406 ΔG_{nps}: nonpolar solvation free energy; ΔG_{bind}: total binding free energy. All values represent mean
407 ± SD.
408
409 To systematically delineate how target recognition modulates the nanoparticle encounter landscape,
410 paired all-atom MD simulations were performed for both apo-RNAm4 and the holo-RNAm4–
411 ceramide complex in the presence of an AuNP. For each system, 20 independent starting
412 configurations were generated by randomly distributing citrate-capped AuNPs along the peripheral
413 contour of the RNA scaffold at a uniform initial minimum distance of 1.5 Å. To ensure strict
414 comparability, the initial approach vectors and center-of-mass positions of the AuNPs were
415 identically matched between the apo and holo regimes (Fig. 4A and B). Across most sampled
416 surface regions, apo-RNAm4 and the RNAm4–ceramide complex exhibited broadly comparable
417 interaction profiles. Notable divergences in AuNP approach behavior were confined to the spatial
418 neighborhood of residues 5U, 7A, 13A, 14A, 21C, and 22U, where the bound ceramide was
419 positioned to potentially perturb interfacial accessibility. Because the 5U region remained
420 sterically inaccessible throughout all 20 trajectories and the 13A domain proved intrinsically non-
421 permissive to AuNP association, representative approach vectors centered around 7A, 14A, 21C,
422 and 22U were selected for in-depth comparative trajectory analysis.

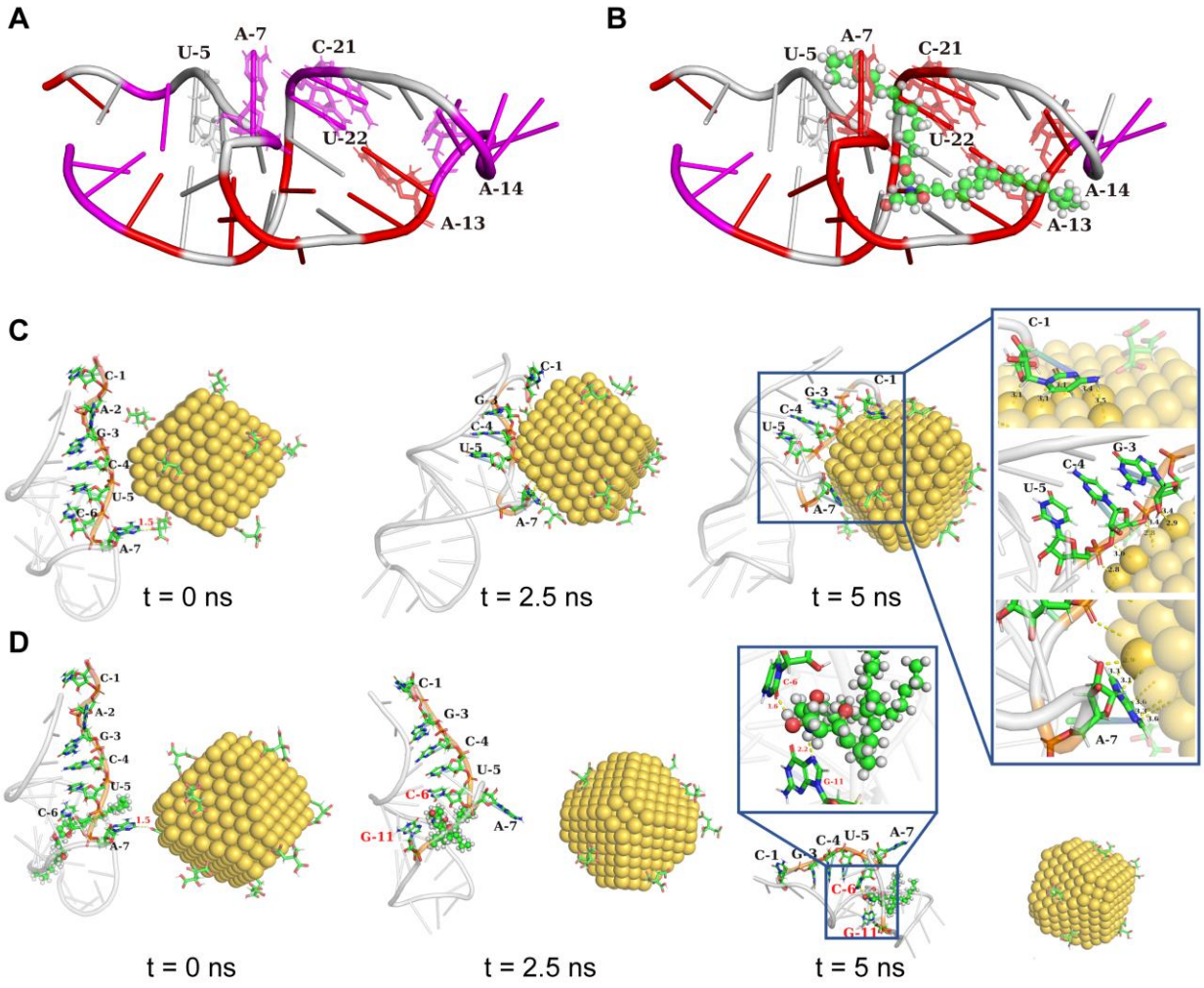


Fig. 4 Atomistic MD simulations demonstrate that target binding to RNAm4 sterically impairs AuNP interfacial passivation. (A, B) Surface distribution of RNA–AuNP encounter competencies across 20 independent 5-ns MD trajectories for (A) apo-RNAm4 and (B) the RNAm4–ceramide complex. Purple envelopes designate binding-permissive patches, red indicates non-binding regimes governed by electrostatic repulsion, and gray denotes unsampled areas. (C) MD simulation trajectory snapshot of apo-RNAm4 approaching an AuNP from the 7A region, showing coplanar nucleobase interations. (D) Representative MD trajectory snapshot of the RNAm4–ceramide complex under the same 7A AuNP initial approach configuration, illustrating steric occlusion by the outward-projecting ceramide aliphatic chains.

As illustrated in Fig. 4C, when the AuNP approached the 7A region of apo-RNAm4 at an initial separation of 1.5 Å, electrostatic repulsion between the polyanionic RNA backbone and surface-bound citrates initially widened the interfacial gap while driving lateral citrate redistribution across the gold facets. Concurrently, conformational adaptation of the flexible loop region guided the 7A nucleobase and neighboring residues toward the newly exposed gold facets. Once the unpaired bases accessed the metallic surface, nitrogen and exocyclic oxygen atoms readily formed stable, coplanar Au–N and Au–O contacts, facilitating spontaneous RNA adsorption and surface passivation (Fig. 4C). In stark contrast, in the holo-RNAm4–ceramide complex (Fig. 4D), despite comparable conformational adjustments within the RNA backbone, the outward-projecting hydrophobic hydrocarbon chains of C16-ceramide occupied the critical interfacial void between the RNA and the AuNP. This steric occlusion prevented the nanoparticle from approaching closely and precluded adjacent nucleobases from establishing planar gold contacts, thereby markedly attenuating RNA-mediated colloidal protection (Fig. 4D). Similar paired trajectory comparisons centered at other representative approach vectors—including residues 21C (Fig. S4), 22U (Fig. S5), and 14A (Fig. S6)—corroborated this target-dependent steric displacement mechanism.

In summary, mechanism-informed engineering of RNA052 yielded RNAm4 as an optimal aptasensor candidate. The established computational pipeline integrates four criteria: target affinity, bound ligand topology, apo-state colloidal stabilization, and target-dependent interfacial occlusion. This design validates the core biophysical mechanism of adsorption-mediated colorimetric aptasensors: flexible apo-aptamers stabilize citrate-capped AuNPs against salt-induced aggregation via nucleobase interactions, while target binding sterically blocks interfacial access, releasing the protection and driving a target-responsive optical readout.

Experimental Validation Demonstrates Target-Dependent Colorimetric Detection and Confirms the Prioritization Cascade

To experimentally validate the computational selection workflow, the prioritized candidate aptamer was evaluated using an AuNP-based colorimetric assay, benchmarking against the parent scaffold RNA052. As hypothesized, the RNAm4–AuNP system exhibited a distinct color transition from wine-red to purple/blue with increasing C16-ceramide concentrations (Fig. 5A). Consistent with this visual observation, UV–vis absorption spectra revealed a concentration-dependent decrease in the characteristic plasmon absorption band near 520 nm, accompanied by an increased relative contribution of long-wavelength absorbance (Fig. 5C) In contrast, the RNA052–AuNP system displayed no noticeable optical or spectral response across the identical target concentration regime (Fig. 5B and D). This difference in colorimetric response directly corroborates our simulation predictions. Furthermore, challenging RNAm4 with structural analogues harboring elongated acyl chains—specifically C18-ceramide (Fig. S7A) and C24-ceramide (Fig. S7B)—elicited negligible color transition under identical assay conditions. This lack of cross-reactivity supports RNAm4's target specificity for C16-ceramide, establishing it as an effective synthetic aptamer for colorimetric detection.

To further substantiate the need for our dual-descriptor screening criterion, we evaluated the negative-control sequences RNA023 (Fig. S7C) and RNAm2 (Fig. S7D) in the colorimetric assay. RNA023 represents an unengineered candidate with an outward-oriented ceramide-binding pose but an unfavorable positive binding free energy ($\Delta G_{bind} = +23.353\ kJ \cdot mol^{-1}$, Table 1), whereas mutant RNAm2 retained favorable binding thermodynamics ($\Delta G_{bind} = -286.397\ kJ \cdot mol^{-1}$, Table 2) but lacked the requisite outward-facing steric display. Notably, neither RNA023 nor RNAm2 showed a detectable colorimetric response as C16-ceramide concentration increased. These negative outcomes further support our design principle that high thermodynamic affinity or outward ligand presentation alone can be insufficient; robust signal transduction in adsorption-mediated colorimetric aptasensors requires the integration of both criteria.

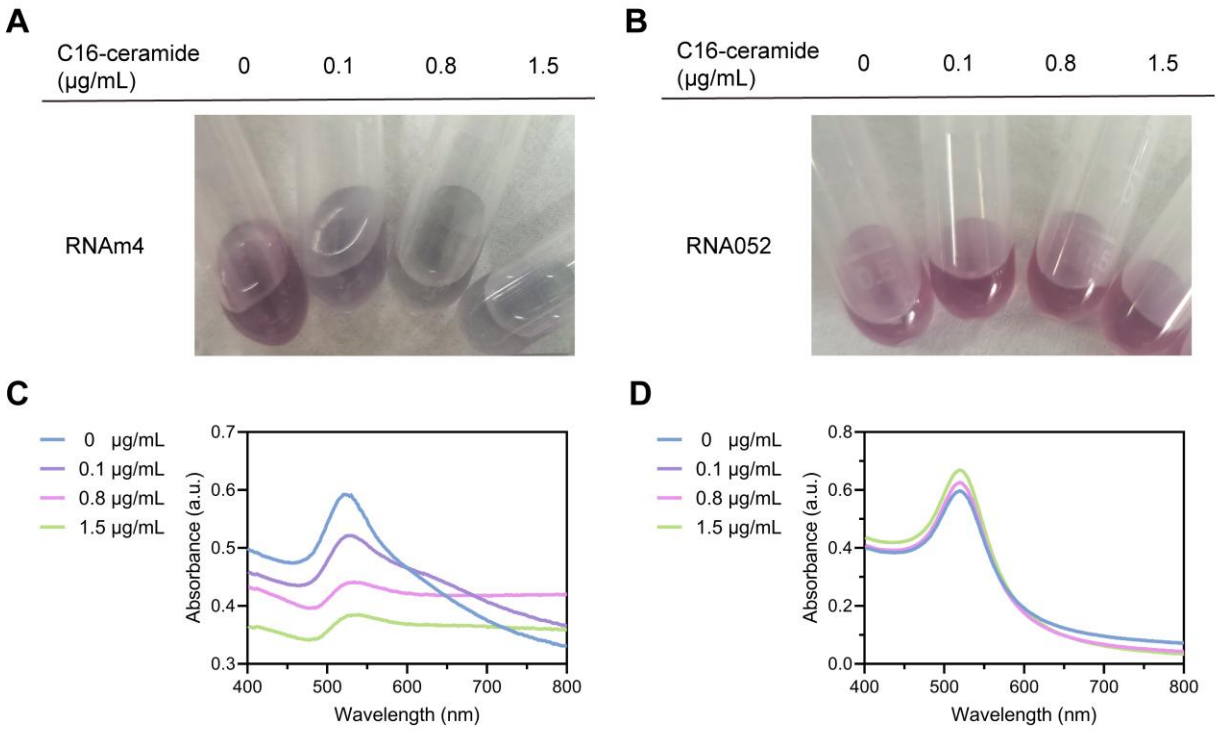


Fig. 5 Experimental colorimetric validation confirms RNAm4 as a functional aptamer for AuNP-based C16-ceramide sensing. (A-B) Visual colorimetric response of the AuNP–RNAm4 (A) and AuNP–RNA052 (B) systems at varying C16-ceramide concentrations. (C-D) UV–vis absorption spectra of the AuNP–RNAm4 (C) and AuNP–RNA052 (D) systems at varying C16-ceramide concentrations.

Conclusion

In this work, we established and experimentally validated a mechanism-driven computational framework for the rational prioritization and mechanism-informed design of RNA aptamers tailored specifically for unmodified AuNP-based colorimetric biosensing, using C16-ceramide as a challenging hydrophobic small-molecule target. Conventional *in vitro* SELEX or *in silico* screening workflows predominantly optimize thermodynamic binding affinity, frequently overlooking the structural and interfacial requirements essential for downstream signal

transduction. By orchestrating secondary-structure complexity filtering, thermodynamic binding free energy calculations, ligand-docking topology profiling, and all-atom RNA–AuNP encounter simulations, our approach directly interrogates the dynamic interfacial behavior of candidate sequences at both the target-binding and nanoparticle-passivating interfaces. Although parent RNA052 exhibited the strongest intrinsic affinity, its inside-the-helix binding mode deeply sequestered the lipid tails within the helical groove, preventing target-dependent modulation of colloidal protection. Targeted loop remodeling successfully generated RNAm4, which preserved favorable binding thermodynamics while adopting an outward-oriented spatial display of the ceramide hydrocarbon chains. This outward protrusion sterically blocks essential nucleobase–gold coplanar contacts upon target complexation, thereby weakening RNA-mediated colloidal stabilization and promoting salt-induced AuNP aggregation.

This computational strategy establishes an actionable design paradigm for adsorption-mediated optical biosensors by moving beyond traditional affinity-only selection criteria. By integrating target-binding stability with steric regulation of nanoparticle-adsorbing interfaces, our framework directly bridges computational modeling and practical colloidal surface chemistry. These findings provide biophysical insight into the competitive interplay among electrostatic repulsion, ligand reorganization, and nucleobase chemisorption that governs non-thiolated nucleic acid behavior on citrate-capped metallic surfaces. Ultimately, this mechanism-informed prioritization pipeline provides a blueprint that complements experimental SELEX and accelerates the *de novo* engineering of label-free colorimetric aptasensors for diverse small-molecule targets.

Data Availability

No datasets were generated or analysed during the current study.

Acknowledgements

Funding: The authors received no specific funding for this work.

Author Contributions

Conceptualization, Y.L. and D.M.; methodology, Y.L. and D.M.; validation, H.C., Y.L. and D.M.; formal analysis, H.C., Y.L. and D.M.; investigation, H.C., Y.L., Y.Y. and D.M.; writing—original draft preparation, H.C., Y.L. and D.M.; writing—review and editing, H.C., Y.L. and D.M.; visualization, H.C and Y.L.; supervision, D.M. and Y.Y.; project administration, D.M. and Y.Y.; funding acquisition, D.M.. All authors read and approved the final manuscript.

Statements and Declarations

Conflict of interest

The authors declare no conflict of interest.

Reference

1. Hermann, T. and D.J. Patel, Biochemistry - Adaptive recognition by nucleic acid aptamers. Science, 2000. 287(5454): p. 820-825.
2. Ellington, A.D. and J.W. Szostak, In vitro selection of RNA molecules that bind specific ligands. Nature, 1990. 346(6287): p. 818-22.
3. McKeague, M. and M.C. Derosa, Challenges and opportunities for small molecule aptamer development. J Nucleic Acids, 2012. 2012: p. 748913.
4. Singh, N.K., et al., High-affinity one-step aptamer selection using a non-fouling porous hydrogel. Nat Biotechnol, 2024. 42(8): p. 1224-1231.

5. Wrzesinski, J. and J. Ciesiolka, Characterization of structure and metal ions specificity of Co2+-binding RNA aptamers. Biochemistry, 2005. 44(16): p. 6257-68.
6. Tan, J.H. and A.G. Fraser, Quantifying metabolites using structure-switching aptamers coupled to DNA sequencing. Nat Biotechnol, 2026. 44(1): p. 60-63.
7. Alkhamis, O., et al., High-Affinity Aptamers for In Vitro and In Vivo Cocaine Sensing. J Am Chem Soc, 2024. 146(5): p. 3230-3240.
8. Song, K.M., S. Lee, and C. Ban, Aptamers and their biological applications. Sensors (Basel), 2012. 12(1): p. 612-31.
9. Ruscito, A. and M.C. DeRosa, Small-Molecule Binding Aptamers: Selection Strategies, Characterization, and Applications. Front Chem, 2016. 4: p. 14.
10. Sadiq, Z., et al., Gold Nanoparticles-Based Colorimetric Assays for Environmental Monitoring and Food Safety Evaluation. Crit Rev Anal Chem, 2024. 54(7): p. 2209-2244.
11. Li, H. and L. Rothberg, Colorimetric detection of DNA sequences based on electrostatic interactions with unmodified gold nanoparticles. Proc Natl Acad Sci U S A, 2004. 101(39): p. 14036-9.
12. Phanchai, W., et al., Insight into the Molecular Mechanisms of AuNP-Based Aptasensor for Colorimetric Detection: A Molecular Dynamics Approach. Langmuir, 2018. 34(21): p. 6161-6169.
13. Lunnoo, T., et al., DNA-Based Gold Nanoparticle Sensor for Bladder Cancer Detection. ACS Applied Nano Materials, 2022. 5(1): p. 985-995.
14. Zhang, F. and J. Liu, Interactions of the Cocaine and Quinine Aptamer with Gold Nanoparticles under the Dilute Biosensor and Concentrated NMR Conditions. Langmuir, 2021. 37(40): p. 11939-11947.
15. Tuerk, C. and L. Gold, Systematic Evolution of Ligands by Exponential Enrichment - Rna Ligands to Bacteriophage-T4 DNA-Polymerase. Science, 1990. 249(4968): p. 505-510.
16. Merrill, A.H., Jr., Sphingolipid and glycosphingolipid metabolic pathways in the era of sphingolipidomics. Chem Rev, 2011. 111(10): p. 6387-422.

17. Han, X., et al., Metabolomics in early Alzheimer's disease: identification of altered plasma sphingolipidome using shotgun lipidomics. PLoS One, 2011. 6(7): p. e21643.
18. Moseholm, K.F., et al., Circulating sphingolipids in relation to cognitive decline and incident dementia: The Cardiovascular Health Study. Alzheimers Dement (Amst), 2024. 16(3): p. e12623.
19. Horii, K., et al., Development of a sphingosylphosphorylcholine detection system using RNA aptamers. Molecules, 2010. 15(8): p. 5742-55.
20. Lorenz, R., et al., ViennaRNA Package 2.0. Algorithms Mol Biol, 2011. 6: p. 26.
21. Watkins, A.M., R. Rangan, and R. Das, FARFAR2: Improved De Novo Rosetta Prediction of Complex Global RNA Folds. Structure, 2020. 28(8): p. 963-976 e6.
22. Kim, S., et al., PubChem 2025 update. Nucleic Acids Res, 2025. 53(D1): p. D1516-D1525.
23. Allinger, N.L., Conformational analysis. 130. MM2. A hydrocarbon force field utilizing V1 and V2 torsional terms. Journal of the American Chemical Society, 1977. 99(25): p. 8127-8134.
24. Eberhardt, J., et al., AutoDock Vina 1.2.0: New Docking Methods, Expanded Force Field, and Python Bindings. J Chem Inf Model, 2021. 61(8): p. 3891-3898.
25. Morris, G.M., et al., AutoDock4 and AutoDockTools4: Automated docking with selective receptor flexibility. J Comput Chem, 2009. 30(16): p. 2785-91.
26. Ming, D., J.D. Cohn, and M.E. Wall, Fast dynamics perturbation analysis for prediction of protein functional sites. BMC Struct Biol, 2008. 8: p. 5.
27. Abraham, M.J., et al., GROMACS: High performance molecular simulations through multi-level parallelism from laptops to supercomputers. SoftwareX, 2015. 1-2: p. 19-25.
28. Perez, A., et al., Refinement of the AMBER force field for nucleic acids: improving the description of alpha/gamma conformers. Biophys J, 2007. 92(11): p. 3817-29.
29. Zgarbová, M., et al., Refinement of the Cornell et al. Nucleic Acids Force Field Based on Reference Quantum Chemical Calculations of Glycosidic Torsion Profiles. Journal of Chemical Theory and Computation, 2011. 7(9): p. 2886-2902.

30. Wang, J., et al., Development and testing of a general amber force field. J Comput Chem, 2004. 25(9): p. 1157-74.
31. Jakalian, A., D.B. Jack, and C.I. Bayly, Fast, efficient generation of high-quality atomic charges. AM1-BCC model: II. Parameterization and validation. Journal of Computational Chemistry, 2002. 23(16): p. 1623-1641.
32. Jorgensen, W.L., et al., Comparison of simple potential functions for simulating liquid water. The Journal of Chemical Physics, 1983. 79(2): p. 926-935.
33. Darden, T., D. York, and L. Pedersen, Particle mesh Ewald: An N·log(N) method for Ewald sums in large systems. The Journal of Chemical Physics, 1993. 98(12): p. 10089-10092.
34. Hess, B., et al., LINCS: A linear constraint solver for molecular simulations. Journal of Computational Chemistry, 1997. 18(12): p. 1463-1472.
35. Kumari, R., et al., g_mmpbsa--a GROMACS tool for high-throughput MM-PBSA calculations. J Chem Inf Model, 2014. 54(7): p. 1951-62.
36. Baker, N.A., et al., Electrostatics of nanosystems: application to microtubules and the ribosome. Proc Natl Acad Sci U S A, 2001. 98(18): p. 10037-41.
37. Eisenhaber, F., et al., The double cubic lattice method: Efficient approaches to numerical integration of surface area and volume and to dot surface contouring of molecular assemblies. Journal of Computational Chemistry, 1995. 16(3): p. 273-284.
38. Wang, J., et al., Automatic atom type and bond type perception in molecular mechanical calculations. J Mol Graph Model, 2006. 25(2): p. 247-60.
39. Berendsen, H.J.C., J.R. Grigera, and T.P. Straatsma, The missing term in effective pair potentials. The Journal of Physical Chemistry, 1987. 91(24): p. 6269-6271.
40. Miyamoto, S. and P.A. Kollman, Settle: An analytical version of the SHAKE and RATTLE algorithm for rigid water models. Journal of Computational Chemistry, 1992. 13(8): p. 952-962.
41. Bayly, C.I., et al., A well-behaved electrostatic potential based method using charge restraints for deriving atomic charges: the RESP model. The Journal of Physical Chemistry,

1993. 97(40): p. 10269-10280.

42. Sousa da Silva, A.W. and W.F. Vranken, ACPYPE - AnteChamber PYthon Parser interfacE. BMC Res Notes, 2012. 5: p. 367.

43. Liu, J. and Y. Lu, Preparation of aptamer-linked gold nanoparticle purple aggregates for colorimetric sensing of analytes. Nat Protoc, 2006. 1(1): p. 246-52.

44. Turkevich, J., P.C. Stevenson, and J. Hillier, A study of the nucleation and growth processes in the synthesis of colloidal gold. Discussions of the Faraday Society, 1951. 11: p. 55-75.

45. Haiss, W., et al., Determination of size and concentration of gold nanoparticles from UV-vis spectra. Anal Chem, 2007. 79(11): p. 4215-21.

46. Chushak, Y. and M.O. Stone, In silico selection of RNA aptamers. Nucleic Acids Res, 2009. 37(12): p. e87.

47. Zhang, X., M.R. Servos, and J. Liu, Surface science of DNA adsorption onto citrate-capped gold nanoparticles. Langmuir, 2012. 28(8): p. 3896-902.

48. Acioli, P.H. and S. Srinivas, Silver- and gold-mediated nucleobase bonding. J Mol Model, 2014. 20(8): p. 2391.

49. Zhang, X., C.Q. Sun, and H. Hirao, Guanine binding to gold nanoparticles through nonbonding interactions. Phys Chem Chem Phys, 2013. 15(44): p. 19284-92.

Supplementary Files

This is a list of supplementary files associated with this preprint. Click to download.

- SupplementaryFiguresMechanismInformedComputationalDesignofRNAAptamersforUnmodifiedAuNPColorimetricSensingofC16Ceramide.pdf